

Symmetry-controlled time structure of high-harmonic carrier fields from a solid

F. Langer¹, M. Hohenleutner¹, U. Huttner^{2,3}, S. W. Koch², M. Kira^{2,3*}, and R. Huber^{1*}

¹*Department of Physics, University of Regensburg, 93040 Regensburg, Germany*

²*Department of Physics, University of Marburg, 35032 Marburg, Germany*

³*Department of Electrical Engineering and Computer Science, University of Michigan, Ann Arbor,
Michigan 48109, USA*

*Authors to whom correspondence should be addressed

High-harmonic (HH) generation in crystalline solids¹⁻⁶ marks an exciting development, with potential applications in high-efficiency attosecond sources⁷, all-optical bandstructure reconstruction^{8,9}, and quasiparticle collisions^{10,11}. Although the spectral¹⁻⁴ and temporal shape⁵ of the HH intensity has been described microscopically^{1-6,12}, the properties of the underlying HH carrier wave have remained elusive. Here we analyse the train of HH waveforms generated in a crystalline solid by consecutive half cycles of the same driving pulse. Extending the concept of frequency combs¹³⁻¹⁵ to optical clock rates, we show how the polarization and carrier-envelope phase (CEP) of HH pulses can be controlled by crystal symmetry. For some crystal directions, we can separate two orthogonally polarized HH combs mutually offset by the driving frequency to form a comb of even and odd harmonic orders. The corresponding CEP of successive pulses is constant or offset by π , depending on the polarization. In the context of a quantum description of solids, we identify novel capabilities for polarization- and phase-shaping of HH waveforms that cannot be accessed with gaseous sources.

Frequency combs¹³ are a central concept of ultrafast photonics and metrology^{14,15}. A train of light pulses (e.g. from a mode-locked laser) with a repetition rate ν_{rep} gives rise to a spectrum consisting of a regular comb of equidistant lines spaced at ν_{rep} . The latter typically lies in the radio to microwave frequency range^{16,17}. If the phase of the carrier wave relative to the maximum of the pulse envelope, the CEP, is constant throughout the entire train, the lowest-frequency comb line is locked to zero¹⁸. A nonzero phase slip in successive pulses, in contrast, manifests itself in an overall shift of the frequency comb by the carrier-envelope offset (CEO) frequency ν_{CEO} .

Phase-locked light pulses ($\nu_{\text{CEO}} = 0$) feature a well-defined optical waveform, which delivers the high precision needed, e.g., in strong-field light-matter interactions^{1-6,8-12,19-25} and attosecond science^{19-21,23-24}. Recently, the carrier wave of infrared and visible pulses has been used to control inter- and intraband quantum motion of electrons in bulk solids^{5,11}, resulting in the generation of HHs. If generated by phase-locked waveforms, the HH pulses feature a constant CEP between subsequent laser shots². In addition, solid-based HH radiation created by multi-cycle mid-infrared transients has been shown to be structured as a sequence of light bursts synchronized with the field crests of the driving waveform^{5,9}.

Here, we extend the concept of frequency combs to a train of HH waveforms generated in a bulk semiconductor within the duration of a single phase-locked multi-terahertz (THz) driving pulse of frequency ν_{THz} . We go beyond studies of the intensity envelope⁵ and analyse the polarization and the CEP slip between HH pulses emerging in consecutive THz half cycles. The symmetry for specific crystal directions determines whether the HH radiation is emitted as nearly identical pulses at repetition rate ν_{THz} or as two orthogonally polarized pulses each featuring a repetition rate of $2\nu_{\text{THz}}$ and a sign flip between consecutive pulses. Therefore, the crystal symmetry can be exploited to control the CEP slip and the polarization at optical clock rates – a capability that is not intrinsically available with atoms and molecules.

As a prototypical crystal supporting efficient HH generation (HHG), we study gallium selenide (GaSe). This semiconductor consists of a van-der-Waals stack of monolayers, each of which is composed of two covalently bound sheets of gallium atoms, sandwiched between two sheets of

selenium. The symmetry group D_3^h of the polytype ε -GaSe used here (A-B stacking) is also represented by a single GaSe monolayer (see Fig. 1a), which exhibits a three-fold rotational axis (c -axis) and a horizontal mirror plane (perpendicular to the c -axis), but no inversion centre. In the honeycomb lattice, the three equivalent vectors \mathbf{e}_1 , \mathbf{e}_2 , and \mathbf{e}_3 (Fig. 1a, arrows) that point along the bonds connecting a selenium with its neighbouring gallium atoms indicate the ‘armchair directions’, whereas the ‘zigzag directions’ (e.g. $\mathbf{e}_1 - \mathbf{e}_2$) line up with the vector connecting nearest atoms of the same species.

In order to generate HH radiation, we focus linearly polarized, intense few-cycle THz pulses with a central frequency of $\nu_{\text{THz}} = 33$ THz (see Supplementary Figure 1) at perpendicular incidence onto a free-standing c -cut GaSe window with a thickness of 40 μm . The peak THz electric field in the focus amounts to 47 MV/cm. For reasons of symmetry, THz excitation along the three equivalent armchair directions \mathbf{e}_1 , \mathbf{e}_2 , and \mathbf{e}_3 (Fig. 1a, arrows) must generate identical HH emission. Therefore, the complete polarization dependence of HHG can be determined by varying the THz polarization direction between \mathbf{e}_1 and $-\mathbf{e}_2$ (Fig. 1a, shaded sector). We denote the THz polarization with respect to the crystal lattice with the crystal angle φ , and choose $\varphi = 0^\circ$ to match the zigzag direction $\mathbf{e}_1 - \mathbf{e}_2$, which is in the middle of the above sector. With this choice, $\varphi = -30^\circ$ ($+30^\circ$) refers to the situation where the THz field lines up with \mathbf{e}_1 ($-\mathbf{e}_2$). Figure 1b shows the polarization-integrated HH spectra as a function of φ in the range $-30^\circ \leq \varphi < +30^\circ$. A full 360° scan (see Supplementary Figure 2) confirms the six-fold symmetry of the HH intensity repeating the pattern defined in Fig. 1b. The intensity is strongest if the THz field points along the bond directions (e.g., $\varphi = \pm 30^\circ$). For intermediate angles, the intensity is reduced but still encompasses both even and odd orders.

The orientation of the crystal and hence the angle φ is readily confirmed by second-harmonic (SH) generation²⁶ since this process requires a broken inversion symmetry, which in GaSe occurs most strongly along the armchair directions $\pm\mathbf{e}_1$, $\pm\mathbf{e}_2$, and $\pm\mathbf{e}_3$ (see Supplementary Information for details). The inner graph of Fig. 1b shows the measured SH intensity $I_{\text{SH},\parallel}$ and $I_{\text{SH},\perp}$ polarized along (red spheres) and perpendicular to (blue spheres) the THz field, respectively. Indeed, $I_{\text{SH},\parallel}$ reaches its

maximum for $\varphi = \pm 30^\circ$, while it vanishes along the inversion symmetric zigzag direction $\varphi = 0^\circ$. Conversely, the perpendicular component $I_{\text{SH},\perp}$ attains its highest value for $\varphi = 0^\circ$ as the symmetry is broken perpendicularly to this crystal direction.

To determine the HH polarization, we measure the intensity of even and odd orders as a function of the polarization angle θ between the HH and the THz field for the special crystal directions $\varphi = -30^\circ$ (Fig. 1c) and $\varphi = 0^\circ$ (Fig. 1d). Evidently, the polarization direction of even harmonic orders (red spheres) switches from parallel ($\varphi = -30^\circ$) to perpendicular ($\varphi = 0^\circ$) to the driving field, in analogy with the SH, whereas odd harmonics at $\varphi = \pm 30^\circ$ and 0° (black spheres) are always polarized along the THz field. Hence, the crystal symmetry not only influences the HH efficiency but also selectively rotates the polarization of even harmonic orders. Similar observations have been made in monolayer molybdenum disulphide²⁷.

While the angular dependence of HHG in MgO has been modelled with semiclassical electron trajectories²⁸, non-perturbative quantum interferences between three or more electronic bands must be included to rigorously explain the generation of even harmonic orders and HH emission for only one polarity of the driving field in GaSe^{2,5}. This mechanism depends on the balancing of different interband excitation pathways mediated by material- and frequency dependent dipole matrix elements and requires a broken inversion symmetry and a non-perturbative excitation⁵. Additionally, the HH polarization direction is conserved only along the bonds \mathbf{e}_1 , \mathbf{e}_2 , and \mathbf{e}_3 of GaSe (Fig. 1). As demonstrated in Refs. 2 and 5, the corresponding excitations can be reduced to a polarization-conserving and effectively one-dimensional dynamics in reciprocal space, as long as one fully includes non-perturbative quantum interferences. This reduction must be generalized for an electric field that significantly excites electrons along multiple bond directions. We find that such a situation can be described by a linear combination of three effectively one-dimensional excitation components associated with the \mathbf{e}_1 , \mathbf{e}_2 , and \mathbf{e}_3 directions (see Supplementary Information). The resulting total HH emission does not necessarily conserve the polarization direction because each of these components typically exhibits different nonlinearities and non-perturbative quantum interferences. As representatives for odd and even orders, Fig. 2 compares the computed HH intensity I_{HH} of the 9th (red

curve) and 12th harmonic order (black curve) with the experimental data (spheres) as a function of φ . Our theory quantitatively explains the measured φ -dependence of I_{HH} (Fig. 2a) and the HH polarization angle θ (Fig. 2b). The agreement also holds for other orders (see Supplementary Figure 6). Figure 2b shows that even- and odd-order HHs remain polarized parallel to \mathbf{e}_1 ($-\mathbf{e}_2$) near $\varphi = \pm 30^\circ$. As φ approaches 0° , the polarization of odd harmonics aligns with the THz field whereas even orders are emitted with perpendicular polarization, in accordance with the experimental data (spheres). Therefore, the crystal orientation in solid-based HHG provides an experimentally viable way to set an arbitrary polarization angle between even and odd harmonic orders (see Supplementary Figure 7).

Our quantum theory also allows us to identify the microscopic origin of this polarization selectivity, which is most dramatic at $\varphi = 0^\circ$. For this particular case, the THz field $\mathbf{E}_{\text{THz}} = E \mathbf{e}_1 - E \mathbf{e}_2$ (dashed arrow in Fig. 2d) is perpendicular to \mathbf{e}_3 and has finite components of equal magnitude but opposite sign along \mathbf{e}_1 and \mathbf{e}_2 , driving HH generation only along those bonds. THz excitation over each bond generates both even E_{even} and odd E_{odd} HH fields. Importantly, the HH response equals $E_{\text{even}} + E_{\text{odd}}$ along bond \mathbf{e}_1 and $E_{\text{even}} - E_{\text{odd}}$ along \mathbf{e}_2 , owing to the sign flip in the driving field and the parity difference between even and odd harmonics (see Supplementary Information and Supplementary Figure 3). The relative vectorial directions of even (red arrows) and odd (black arrows) harmonics are also indicated in Fig. 2d along each bond, which shows that linearly coupled excitations (LCE) explain these HH experiments quantitatively, whereas no evidence of a strong nonlinear intermixing of the contributions from individual bond directions is found. The LCE-based vector addition is illustrated in Fig. 2d, and yields the total HHG response, $E_{\text{even}}(\mathbf{e}_1 + \mathbf{e}_2) + E_{\text{odd}}(\mathbf{e}_1 - \mathbf{e}_2)$, where even and odd harmonic orders are polarized perpendicular to and along the driving field, respectively. It is also clear that HH emission is aligned with one of the bonds when the field points in that particular bond direction (Figs. 2c and e), whereas the even and odd harmonics are abruptly separated as $\varphi = 0^\circ$ is approached (Fig. 2b) because individual bond contributions switch their strength nonlinearly (see Supplementary Figure 5). For example, the \mathbf{e}_3 contribution (Fig. 2a, grey dashed line) remains negligible for the φ -range studied here.

The possibility to separate even and odd harmonics by means of their polarization has far-reaching consequences for the temporal emission characteristics. Figure 3 analyses the time structure of the total HH emission by recording the intensity of the sum frequency $I_{\text{SF}}(t)$ between the HH pulses and an 8-fs near-infrared gate (see Supplementary Figure 1) as a function of the delay time t between the two pulses (see Methods). The phase-matching condition implemented in our experiment makes this scheme selectively sensitive to HH radiation that is polarized parallel to the THz field. Figure 3b shows $I_{\text{SF}}(t)$ as a function of the THz field direction φ with respect to the crystal for a constant CEP of the THz pulses. For $\varphi = -30^\circ$ (along \mathbf{e}_1), we observe a HH pulse train containing three main bursts (Fig. 3b and c) which are locked to the positive field crests of the driving waveform (Fig. 3a), due to electronic quantum interference⁵. When the THz field is switched to the $-\mathbf{e}_2$ direction ($\varphi = +30^\circ$), only negative crests of the driving field produce HH bursts (Fig. 3b and c), consistent with the crystal symmetry that renders a rotation by 60° equivalent to an inversion of the field direction. In both \mathbf{e}_1 ($\varphi = -30^\circ$) and $-\mathbf{e}_2$ ($\varphi = 30^\circ$) directions, successive HH pulses are temporally separated by a full THz oscillation period, entailing a frequency comb spaced at ν_{THz} , as indeed observed in Fig. 1b.

An intriguing situation arises for $\varphi = 0^\circ$. Since the HH pulses recorded in Fig. 3d occur for every half cycle of the driving waveform, the corresponding frequency comb should be spaced at $2\nu_{\text{THz}}$. Yet the spectral maxima in Fig. 1b are actually separated by ν_{THz} , containing both even and odd harmonic orders. This apparent contradiction is resolved when polarization is taken into account: even and odd harmonics are emitted with orthogonal polarizations (Figs. 1d and 2b). As the time-resolved data of Fig. 3d tracks HH components polarized parallel to the driving field, it measures selectively odd-order harmonics in this case. Since their spectral maxima are separated by $2\nu_{\text{THz}}$ they are carried by a train of pulses repeating themselves every THz half cycle as experimentally observed in Fig. 3d and quantitatively reproduced by our quantum theory (see Supplementary Figure 4). Consequently, controlling the crystal angle offers a way to modulate the non-perturbative quantum interference experimentally in both the time and frequency domain.

Analysing our results in terms of frequency combs allows us to extract the CEP slip of successive HH bursts emitted within the same driving pulse for the first time to our knowledge. Figure 4b displays a

computed HH time trace for $\varphi = \pm 30^\circ$. In these cases, both even and odd harmonic orders are polarized parallel to the THz field (Fig. 4a), emission occurs every second half cycle of the driving field and, thus, give rise to a spectrum of harmonics spaced at ν_{THz} (Fig. 4d). Since the frequency comb is locked to $\nu_{\text{CEO}} = 0$, we conclude that the CEP of successive pulses must be identical, as is indeed indicated by our calculations (Fig. 4b, blue and green curves). For $\varphi = 0^\circ$, by contrast, the HH emission can be expanded into odd harmonics (black) and even harmonics (red) polarized parallel and perpendicular to the driving field, respectively (Fig. 4c). As measured in Fig. 3d, the pulse train for one polarization direction occurs with a repetition rate of $2\nu_{\text{THz}}$. Our theory not only reproduces this feature, it also proves that the CEP of the pulse train associated with the perpendicular polarization is constant whereas the waveforms emitted with parallel polarization change sign for subsequent THz half cycles. Owing to this property, the perpendicular frequency comb is locked to $\nu_{\text{CEO}} = 0$ while the parallel comb is characterized by $\nu_{\text{CEO}} = \nu_{\text{THz}}$. Consequently, HH emission at $\varphi = 0^\circ$ results in two combs with a spacing of $2\nu_{\text{THz}}$ and orthogonal polarizations that are superimposed and offset by ν_{THz} (Fig. 4e), effectively producing a HH spectrum of even and odd orders.

In conclusion, we have demonstrated how the time structure of the polarization and the CEP slip of HH waveforms (which constitute information beyond the intensity envelope) can be controlled by the crystal symmetry. By effectively suppressing the breaking of the inversion symmetry along some crystal directions, we may selectively modulate the non-perturbative interband interference underlying crystal-based HHG. Our results set a new benchmark for microscopic theories of HHG and afford a novel recipe to custom-tailor HH waveforms at optical clock rates. By tuning the crystal direction and selecting a specific polarization component, we switch between repetition rates ν_{THz} and $2\nu_{\text{THz}}$ and CEP slips equal to 0 and π , which allows us to implement a level of carrier wave control that exceeds the inherent possibilities given by atomic and molecular gases. Going beyond such binary control, we foresee that this concept will also lend itself to a continuous control of the HH vector potential. Whereas circularly polarized HHG in atomic gases requires the simultaneous presence of a circularly polarized fundamental wave and of a counter-circularly polarized second harmonic²⁹, the presence of equivalent dipoles along \mathbf{e}_1 , \mathbf{e}_2 , and \mathbf{e}_3 should allow for circular HHG in a crystal to be driven by the

fundamental wave only. More complex polarization-shaped THz waveforms³⁰ or tailored optical pulses might even reach a complete vectorial pulse synthesis of HHs, leading to novel perspectives in solid-state attosecond photonics.

References

1. Ghimire, S. *et al.* Observation of high-order harmonic generation in a bulk crystal. *Nature Phys.* **7**, 138-141 (2011).
2. Schubert, O. *et al.* Sub-cycle control of terahertz high-harmonic generation by dynamical Bloch oscillations. *Nature Photon.* **8**, 119-123 (2014).
3. Luu, T.T. *et al.* Extreme ultraviolet high-harmonic spectroscopy of solids. *Nature* **521**, 498-502 (2015).
4. Vampa, G. *et al.* Linking high harmonics from gases and solids. *Nature* **522**, 462-464 (2015).
5. Hohenleutner, M. *et al.* Real-time observation of interfering crystal electrons in high-harmonic generation. *Nature* **523**, 572-575 (2015).
6. Ndabashimiye, G. *et al.* Solid-state harmonics beyond the atomic limit. *Nature* **534**, 520-523 (2016).
7. Ghimire, S. *et al.* Generation and propagation of high-order harmonics in crystals. *Phys. Rev. A* **85**, 043836 (2012).
8. Vampa, G. *et al.* All-Optical Reconstruction of Crystal Band Structure. *Phys. Rev. Lett.* **115**, 193603 (2015).
9. Garg, M. *et al.* Multi-petahertz electronic metrology. *Nature* **538**, 359-363 (2016).
10. Zaks, B., Liu, R.B. & Sherwin, M. S. Experimental observation of electron-hole recollisions. *Nature* **483**, 580-583 (2012).
11. Langer, F. *et al.* Lightwave-driven quasiparticle collisions on a subcycle timescale. *Nature* **533**, 225-229 (2016).
12. Higuchi, T., Stockman, M.I. & Hommelhoff, P. Strong-Field Perspective on High-Harmonic Radiation from Bulk Solids. *Phys. Rev. Lett.* **113**, 213901 (2014).
13. Eckstein, J.N., Ferguson, A.I. & Hänsch, T.W. High-Resolution Two-Photon Spectroscopy with Picosecond Light Pulses. *Phys. Rev. Lett.* **40**, 847-850 (1978).
14. Udem, Th., Holzwarth, R. & Hänsch, T.W. Optical frequency metrology. *Nature* **416**, 233-237 (2002).
15. Cundiff, S. T. & Ye, J. Colloquium: Femtosecond optical frequency combs. *Rev. Mod. Phys.* **75**, 325-342 (2003).
16. Holzwarth, R. *et al.* Optical Frequency Synthesizer for Precision Spectroscopy. *Phys. Rev. Lett.* **85**, 2264-2267 (2000).
17. Bartels, A., Heinecke, D. & Diddams, S.A. 10-GHz Self-Referenced Optical Frequency Comb. *Science* **326**, 681 (2009).
18. Jones, D.J. *et al.* Carrier-Envelope Phase Control of Femtosecond Mode-Locked Lasers and Direct Optical Frequency Synthesis. *Science* **288**, 635-639 (2000).
19. Baltuška, A. *et al.* Attosecond control of electronic processes by intense light fields. *Nature* **421**, 611-615 (2003).

20. Hentschel, M. *et al.* Attosecond metrology. *Nature* **414**, 509-513 (2001).
21. Goulielmakis, E. *et al.* Attosecond Control and Measurement: Lightwave Electronics. *Science* **317**, 769-775 (2007).
22. Feist, A. *et al.* Quantum coherent optical phase modulation in an ultrafast transmission electron microscope. *Nature* **521**, 200-203 (2015).
23. Corkum, P.B. & Krausz, F. Attosecond science. *Nature Phys.* **3**, 381-387 (2007).
24. Krausz, F. & Stockman, M.I. Attosecond metrology: from electron capture to future signal processing. *Nature Photon.* **8**, 205-213 (2014).
25. Nanni, E.A. *et al.* Terahertz-driven linear electron acceleration. *Nature Commun.* **6**, 8486 (2015).
26. Catalano, I.M., Cingolani, A., Minafra, A. & Paorici, C. Second harmonic generation in layered compounds. *Optics Commun.* **24**, 105-108 (1976).
27. Liu, H. *et al.* High-harmonic generation from an atomically thin semiconductor. *Nature Phys.* advance online publication, 14 November 2016 (doi: 10.1038/nphys3946).
28. You, Y.S., Reis, D.A. & Ghimire, S. Anisotropic high-harmonic generation in bulk crystals. *Nature Phys.* advance online publication, 21 November 2016 (doi: 10.1038/nphys3955).
29. Chen, C. *et al.* Tomographic reconstruction of circularly polarized high-harmonic fields: 3D attosecond metrology. *Sci. Adv.* **2**, e1501333 (2016).
30. Sato, M. *et al.* Terahertz polarization pulse shaping with arbitrary field control, *Nature Photon.* **7**, 724-731 (2013).

Acknowledgements The work in Regensburg was supported by the European Research Council through grant number 305003 (QUANTUMsubCYCLE) as well as by the Deutsche Forschungsgemeinschaft (through grant number HU 1598/2-1 and GRK 1570) and the work in Marburg by the Deutsche Forschungsgemeinschaft (through SFB 1083 and grant number KI 917/2-2 and KI 917/3-1).

Author Contributions F.L., M.H., and R.H. carried out the experiment and analysed the data. U.H., S.W.K., and M.K. developed the quantum-mechanical model and carried out the computations. All authors discussed the results and contributed to the writing of the manuscript.

Author Information Reprints and permissions information is available at www.nature.com/reprints. The authors declare no competing financial interests. Correspondence and requests for materials should be addressed to R.H. (rupert.huber@physik.uni-regensburg.de) or M.K. (mackkira@umich.edu).

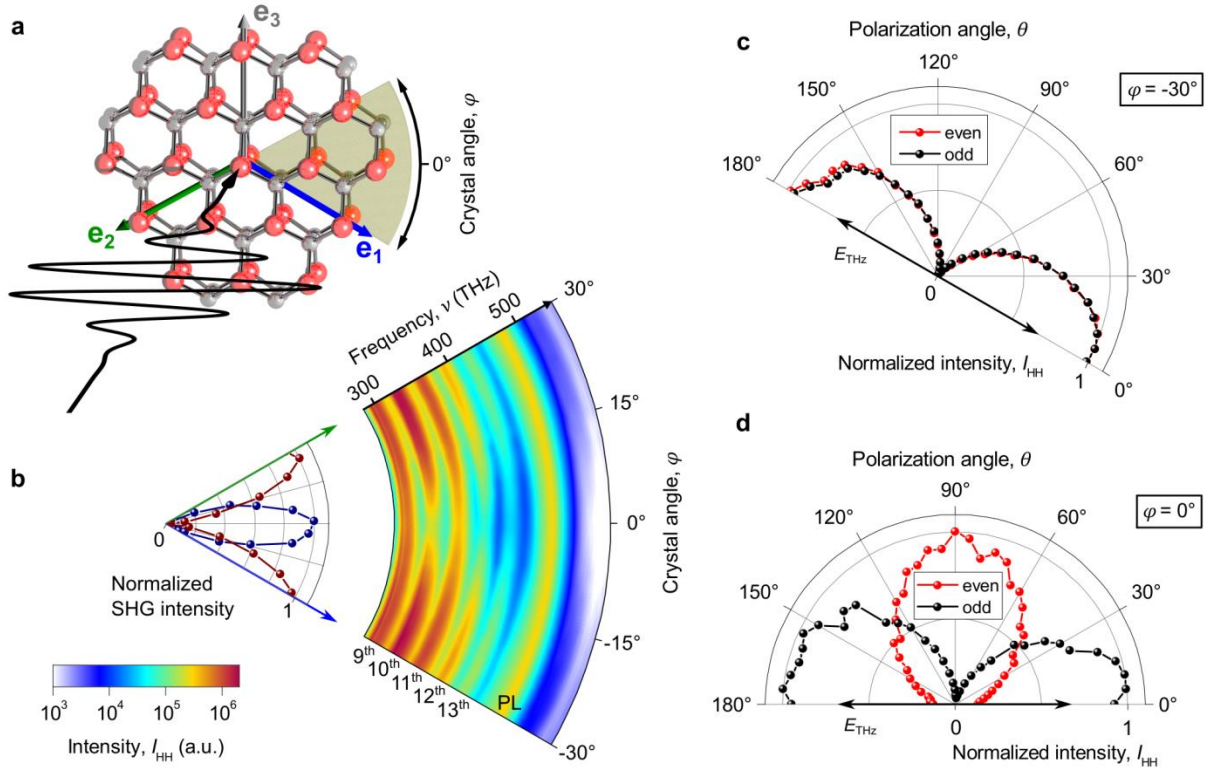


Figure 1 | High-harmonic intensity and polarization for different crystal orientations of gallium selenide. **a**, Top-view of the crystal structure of gallium selenide with the definition of the armchair directions \mathbf{e}_1 , \mathbf{e}_2 , and \mathbf{e}_3 . Gallium atoms are depicted as gray spheres while selenium atoms are red. For HHG, a multi-THz waveform (in black) is focussed onto the GaSe sample under normal incidence. The full symmetry of GaSe is encoded in the 60° -sector shown as a shaded area. **b**, High-harmonic intensity, I_{HH} (colour scale), as a function of the crystal angle φ and frequency ν . The harmonic orders are indicated at the bottom, while PL marks the spectral position of the photoluminescence peak of GaSe. Inner graph: Intensity of second harmonic along different crystal angles φ . The second harmonic component polarized parallel to the fundamental wave (red spheres) features intensity peaks for $\varphi = \pm 30^\circ$, whereas the component polarized perpendicular to the fundamental (blue spheres) is maximal for $\varphi = 0^\circ$. The blue and green arrows indicate the symmetry directions \mathbf{e}_1 and $-\mathbf{e}_2$, respectively. **c**, **d**, High-harmonic intensity of even (red) and odd (black) orders as a function of the polarization angle θ with respect to the fundamental THz field, for $\varphi = -30^\circ$ (**c**) and $\varphi = 0^\circ$ (**d**). The even harmonic orders for $\varphi = 0^\circ$ have a slight residual parallel polarization contribution at $\theta = 0^\circ$ and $\theta = 180^\circ$ because of the spectral overlap with the tails of odd harmonics. The polarization direction of the fundamental driving field is indicated by the double-arrow E_{THz} .

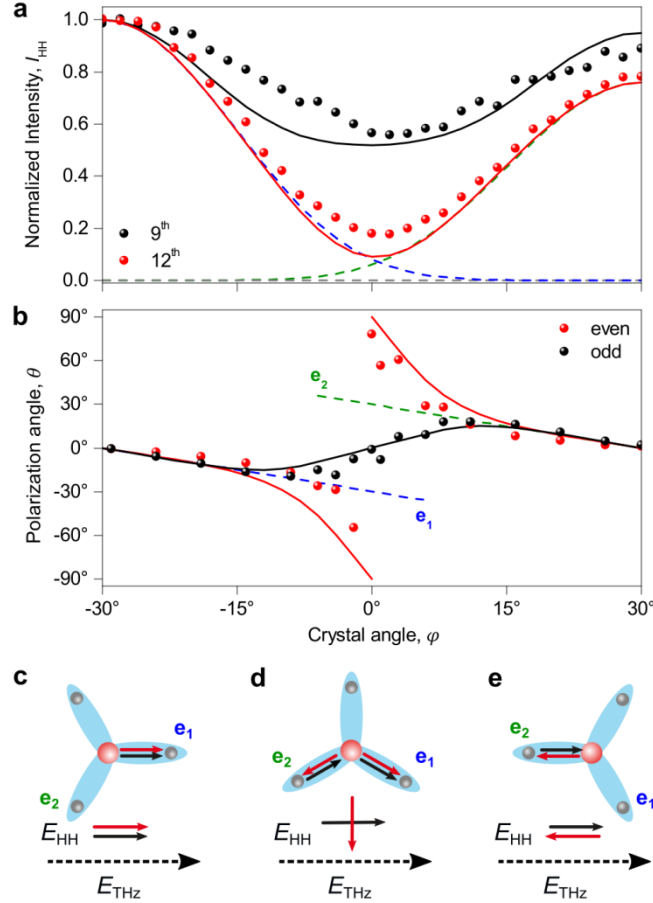


Figure 2 | Crystal-angle dependence of HH generation and comparison between experiment and theory. **a**, Experimental (dots) and calculated (solid curves) high-harmonic intensity of the 9^{th} (black) and 12^{th} (red) harmonic order as a function of the crystal angle φ . The contributions of the three directions e_1 , e_2 , and e_3 to the calculated 12^{th} harmonic are depicted as blue, green, and grey dashed curves, respectively. **b**, Experimentally recorded (dots) and calculated (solid curves) polarization of even-order (red) and odd-order (black) harmonics as a function of the crystal angle φ . The polarization angle $\theta = 0^\circ$ corresponds to a HH polarization aligned with the THz field. For comparison, the directions e_1 and e_2 are shown as blue and green dashed lines, respectively. **c-e**, Schematics of the main contributing crystal directions with their respective dipoles for the special cases $\varphi = -30^\circ$ (**c**), $\varphi = 0^\circ$ (**d**), and $\varphi = 30^\circ$ (**e**). The direction of the red and black arrows labelled E_{HH} depicts the macroscopic polarization of even (E_{even}) and odd (E_{odd}) HHs. The dashed arrow E_{THz} shows the contributing direction of the THz field.

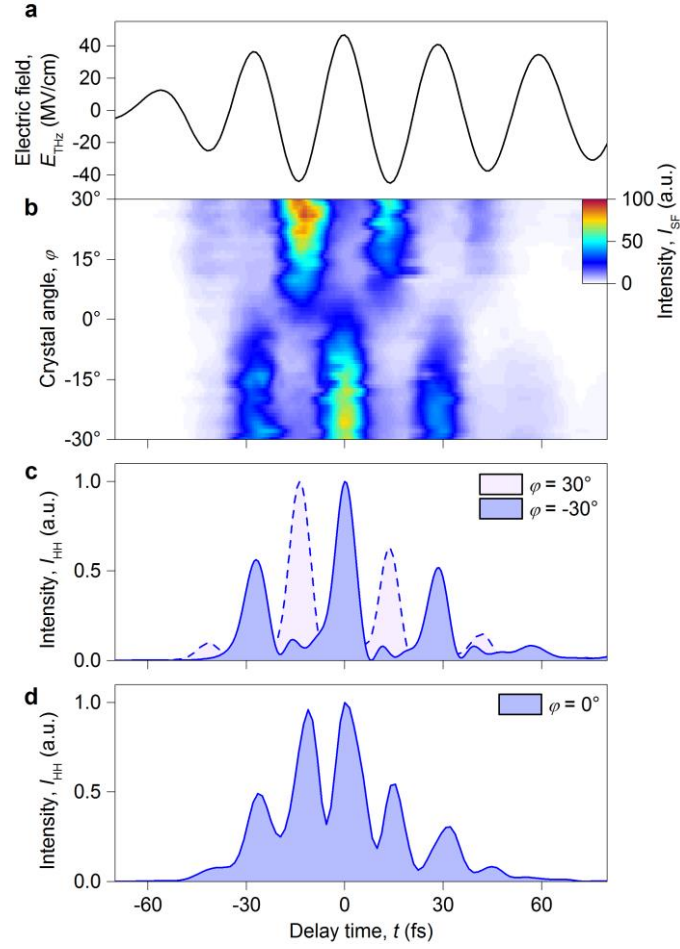


Figure 3 | Subcycle high-harmonic pulse trains generated for different crystal directions. **a**, Electro-optically detected driving THz waveform. The detector response has been accounted for and the temporal axis is directly correlated to the sum-frequency map in **b**. **b**, Sum-frequency intensity I_{SF} (colour scale) from a nonlinear cross-correlation between high-harmonic pulses and an ultrashort gating pulse as a function of delay time t and crystal angle φ . **c**, **d**, Intensity envelopes of HH pulse trains emitted parallel to \mathbf{E}_{THz} reconstructed from a cross-correlation frequency resolved optical gating (XFROG) measurement for crystal angles of $\varphi = \pm 30^\circ$ (**c**) and $\varphi = 0^\circ$ (**d**).

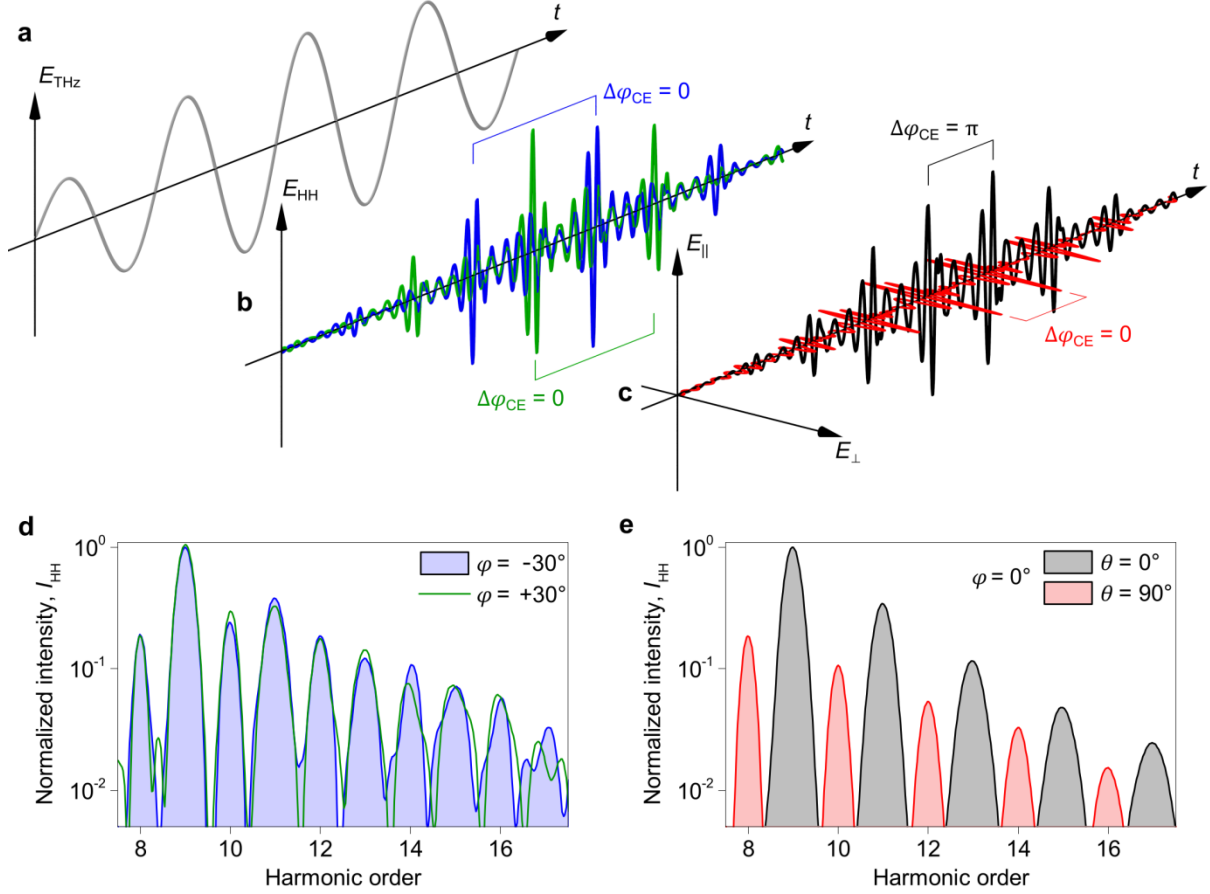


Figure 4 | Time structure of the HH carrier wave. **a**, Waveform E_{THz} of the THz driving field. **b**, **c**, Carrier wave E_{HH} of the high-harmonic pulse train as a function of time containing frequency components above the 7th harmonic order. The data are obtained with the quantum theory described in the text. **b**, For THz excitation along $\varphi = -30^\circ$ (blue solid line) and $\varphi = 30^\circ$ (green solid line), E_{HH} is polarized along E_{THz} (black line in **a**) and the high-harmonic pulses are generated with a repetition rate of ν_{THz} . The carrier envelope phase slip between successive pulses, $\Delta\varphi_{\text{CE}}$, vanishes. **c**, Excitation along $\varphi = 0^\circ$ induces two pulse trains featuring parallel (black solid line) and perpendicular (red solid line) polarization components of E_{HH} with respect to E_{THz} . Both trains occur with a repetition rate of $2\nu_{\text{THz}}$, but with a different carrier envelope phase slips of $\Delta\varphi_{\text{CE}} = \pi$ for the parallel polarization component and $\Delta\varphi_{\text{CE}} = 0$ for the perpendicular polarization component, respectively. **d**, **e**, High-harmonic frequency combs obtained by a Fourier transform of the corresponding pulse trains in **b** and **c**. Whereas a single frequency comb of even- and odd-order harmonics is generated for $\varphi = \pm 30^\circ$ (**d**), the two orthogonally polarized pulse trains generated for $\varphi = 0^\circ$ are linked to two sets of comb lines (**e**, black lines, $\theta = 0^\circ$; red lines, $\theta = 90^\circ$) spaced at $2\nu_{\text{THz}}$, but mutually offset by $\nu_{\text{CEO}} = \nu_{\text{THz}}$.

Methods

Experimental set-up. We generate high harmonics by irradiating a 40- μm -thick crystal of gallium selenide with intense multi-THz pulses. These pulses are obtained by difference frequency mixing of two phase-correlated near-infrared pulse trains from a dual optical parametric amplifier seeded by a titanium sapphire amplifier³¹. The centre frequency is tuneable and set to 33 THz in the experiments. The peak field strength amounts to 47 MV/cm while the pulse duration is approximately 85 fs (full width at half maximum of the intensity envelope). High-harmonic spectra are recorded with a spectrograph employing a thermo-electrically cooled silicon charge-coupled device camera. For polarization-resolved measurements we use a Glan-Thompson polarizer with an extinction ratio of 10^{-5} . Polarization-resolved spectra are corrected for the efficiency of the spectrograph for different polarizations.

Time-resolved measurements of the high-harmonic pulse train are recorded according to the technique introduced in ref. 5. We employ a 10- μm -thick β -barium borate (BBO) crystal to generate the sum frequency component between high harmonics and an 8-fs-long gating pulse from a supercontinuum source as a cross-correlation signal⁵. Established reconstruction algorithms³² are used to extract the HH pulse profile. A direct temporal correlation to the driving field is achieved by electro-optic detection in a 6.5- μm -thick zinc telluride crystal, accounting for the detector response³³ as well as for the Gouy phase shift³⁴.

Data availability. The data that support the plots within this paper and other findings of this study are available from the corresponding author upon reasonable request.

References

31. Sell, A., Leitenstorfer, A. & Huber, R. Phase-locked generation and field-resolved detection of widely tunable terahertz pulses with amplitudes exceeding 100 MV/cm. *Opt. Lett.* **33**, 2767-2769 (2008).
32. Wyatt, A. Frequency-resolved optical gating. (<http://www.mathworks.com/matlabcentral/fileexchange/16235-frequency-resolved-optical-gating--frog->) MATLAB central file exchange, 07.07.2008
33. Gallot, G. & Grischkowsky, D. Electro-optic detection of terahertz radiation. *J. Opt. Soc. Am. B* **16**, 1204-1212 (1999).
34. Ruffin, A. B., Rudd, J.V., Whitaker, J. F., Feng, S. & Winful, H. G. Direct Observation of the Gouy Phase Shift with Single-Cycle Terahertz Pulses. *Phys. Rev. Lett.* **83**, 3410-3413 (1999).